Analysis of Displacement-Controlled Fretting Between a Hemisphere and a Flat Block in Elasto-Plastic Contacts

Huaidong Yang
G. W. Woodruff School of Mechanical Engineering,
Georgia Institute of Technology,
Atlanta, GA 30332-0405
e-mail: hyang380@gatech.edu

Itzhak Green
G. W. Woodruff School of Mechanical Engineering,
Georgia Institute of Technology,
Atlanta, GA 30332-0405
e-mail: green@gatech.edu

This work employs a three-dimensional (3D) finite element analysis (FEA) to investigate the fretting metallic contact between a deformable hemisphere and a deformable flat block. Fretting is governed by displacement-controlled action where the materials of the two contacting bodies are set to have identical properties; studied first is steel-on-steel and then copper-on-copper. At contact onset, a normal interference (indentation) is applied, which is then followed by transverse cyclic oscillations. A large range of coefficients of friction (COFs) is imposed at the interface. The results show that the maximum von Mises stress is confined under the contacting surface for small COFs; however, that maximum reaches the contacting surface when the COFs are sufficiently large. It is also shown that fretting under sufficiently large COFs forms large plastic strains in "ring" like patterns at the contacting surfaces. Junction growth is found where the contacting region is being stretched in the direction of the fretting motion. At large COFs, pileups show up at the edges of the contact. The fretting loops of the initial cycles are found along with the total work invested into the system. At certain interference, there exists a certain COF, which results in the largest work consumption. The magnitude of the COF is found to produce either partial slip (prone for fretting fatigue) or gross slip (prone for fretting wear). A scheme of normalization is proposed, and it is shown to be effective for the two said materials that have vastly different material properties. Hence, the normalized results may well characterize a range of contact scales (from micro to macro) of various ductile material pairs that behave in an elastic–plastic manner with strain hardening. [DOI: 10.1115/1.4041535]

1 Introduction

Fretting is a physical phenomenon that takes place between two surfaces in contact under cyclic motion [1]. It occurs in assemblies of engineering elements with the existence of vibration, cyclic loading or cyclic temperature changes, as well as bearing races and shafts, electrical contacts, reactor elements, turbine engine disks [2–5], etc. Three different regimes of fretting are observed according to the types of the contact conditions: stick, mixed stick–slip, and gross slip [6]. The stick conditions correspond to low damage fretting. The mixed stick–slip conditions mainly result in a fatigue crack formation, while the gross slip conditions are mainly responsible for wear [7]. This work studies the effects of elasto-plastic three-dimensional (3D) spherical contact on the mechanisms of fretting damage, and the propensity for wear, crack initiation, and propagation.

Gordelier and Chivers suggest a method of categorizing the fretting by the loading conditions [8]. A load-controlled condition represents the situation when the force is given while the relative displacement is an output. A displacement-controlled condition represents the situation when the relative displacement is imposed while the force is an output. While practical situations may fall between these two extremes, the loading condition in this work is displacement-controlled as it is in Ref. [9].

The experiments conducted by Courtney-Pratt and Eisner [10] may be of the earliest studies related to the fretting phenomenon. They examine the underlying phase of the oscillatory tangential loading applied at the contact between a metallic sphere and metallic flat surfaces. The hysteresis loop is reported, and the junction growth is indicated by the difference in the electrical conductance. Junction growth is also found by Parker and Hatch [11], and by Tabor [12]. Fretting damage (wear and fatigue) is investigated by increasing the number of loading cycles to the order of thousands or even millions [13–17]. Coatings and lubricant conditions are found to mitigate fretting damage in these works. Some analytical works on fretting contacts are done in Refs. [18–20]. Jin et al. [18] proposed a geometry-independent coefficients of friction (COF) method in a two-dimensional (2D) cylinder-on-flat gross-slip fretting contact. Eriten et al. [19] proposed a physics-based partial slip modeling approach in 3D elastic and elastic–plastic contacts, and they further apply their model to flat rough surfaces [20].

Numerical analyses on fretting initiation start with the study of purely normal contact, where customarily they are done by the finite element analysis (FEA) methodology. The elastic–plastic to fully plastic spherical normal contacts are studied in detail in Refs. [21–23]. The critical values at the onset of plasticity in the contact including the interference, the maximum contact pressure, and the load are found by Jackson and Green [22]. Unidirectional sliding in spherical 3D contacts is investigated numerically by FEA [24–26]. In the model by Holmberg et al. [24], of a rigid sphere pressed against elastic–plastic flat surfaces, ploughing and pileups are apparent in the results. The works of Green [26] investigate the unidirectional sliding contact between two interfering hemispheres. The comparison between the results of FEA and a semi-analytical method (SAM) [27] is made in ample detail in Ref. [26]. While the SAM results show similar trends compared to those obtained from the FEA, the SAM cannot handle dissimilar materials where its results deviate steeply from those obtained by FEA with the increase of the interference (i.e., with the intensifying of strains and the spreading effects of plasticity). The aim in this work is the fretting mechanism and its outcomes. The

Contributed by the Tribology Division of ASME for publication in the JOURNAL OF TRIBOLOGY. Manuscript received June 21, 2018; final manuscript received September 15, 2018; published online November 1, 2018. Assoc. Editor: Wenzhong Wang.

numerical means by which the results are obtained is of a lesser significance. The numerical packages chosen for this investigation (ANSYS and ABAQUS) are tried-and-true, possessing vast arrays of database management and visualization. This is compounded with a meticulous effort undertaken to establish mesh and model convergence.

Fretting fatigue and wear happen under oscillatory motion. Stick and/or slip regions at the contact depend on the normal loading and the traction conditions at the interface. Fretting in 2D cylindrical contact are investigated by FEA in Refs. [28–30]. The model in Refs. [30] and [31] utilizes displacement-controlled fretting conditions between a half cylinder and a flat block having identical [29] and dissimilar [31] material properties. The large von Mises stresses (near the yield strength) and plastic strains are found at the edges of the contact. The junction growth and the pileup at the edges are observed. The 3D fretting contacts are studied in Refs. [32] and [33]. Both works model the contact between a rigid flat and a deformable hemisphere. Zolotarevskiy et al. [32] focused on the full stick and force-controlled conditions. The evolution of the tangential load and the shake down phenomenon are reported. Shi et al. [33] focused on the partial slip condition with both force-controlled and displacement-controlled loadings. The junction growth and shake down are investigated. However, the sliding and gross slip conditions, or scars on the flat are excluded from these two analyses.

The fretting phenomenon is investigated in this work by modeling a 3D contact between a hemisphere and a flat block subject to controlled displacements. The block is sufficiently large and thick to be considered as a half-elastic space. A constant interference is first applied to the top surface of the hemisphere followed then by oscillatory tangential displacements. The current 3D point contact loading (or indentation) is distinctly different from the line contact investigated in Ref. [25]. The material properties of the two contacting bodies are identical. First, steel pairs and later copper pairs, both having 1% strain hardening, are used to test a normalization scheme that is offered. Different coefficient of frictions and interferences are applied in the model. The distribution of the von Mises stresses, plastic strains, deformed surface profiles, junction growth, the evolution of the tangential force, and the work done to the system are reported in this work.

2 The Model

The fretting model represents contact between an oscillating hemisphere and a stationary flat block (Fig. 1). In order to take advantage of the symmetry of the problem, the hemisphere and the block are cut in half along the vertical plane. As shown in Fig. 1(*a*), a quarter sphere with radius $R = 0.5$ m is in contact with a $4R \times 2R \times R$ block. The coordinate system is shown in Figs. 1(*b*) and 1(*c*). For brevity, the positive and negative X directions are implicitly represented by "right" and "left."

Roller boundary conditions of no displacement normal to the plane are applied to the vertically cut plane of the quarter sphere (due to the symmetry with respect to XY plane) and to all the five faces of the block, except to the top face (the XZ plane), which is free to deform in all directions. Such boundary conditions make the block behave as an elastic half space due to the Saint Venant principal, as discussed later.

The hemisphere and the block are set to possess identical material properties, and the reported results are obtained first for a steel-on-steel interface. Later, the case of copper-on-copper is used to generate results for verification of a normalization scheme. The material properties are listed in Table 1. Both materials are assumed to possess a 1% strain hardening based on the elastic modulus. That amount of the tangential modulus is verified not to significantly affect the FEA results, yet it improves the convergence times in ANSYS. The code ABAQUS is used too on select cases just to verify result. Adhesion is not considered in this work.

The fretting model is shown in Fig. 1(*d*). A vertical displacement, ω, is first applied on the top surface of the hemisphere and is kept constant throughout. Then, a following oscillatory horizontal displacement in the X direction, δ, is applied. The hemisphere is initially forced to the "right." The movement is achieved quasi-statically. It takes 40 loading steps to finish one cycle of horizontal displacement. The fretting model in this work is similar to the 2D fretting model in Ref. [30], but here the model is 3D. Some additional details can be found in Ref. [25].

In the regime of static elastic normal contact, the Hertzian theory gives the solution to the 3D spherical contact [34]. Given a normal load, P, the contact radius, a, is obtained by

$$a = \left(\frac{3PR}{4E'}\right)^{\frac{1}{3}} \tag{1}$$

E' is the equivalent elastic modulus

$$\frac{1}{E'} = \frac{1-\nu_1^2}{E_1} + \frac{1-\nu_2^2}{E_2} \tag{2}$$

Since the material properties of the hemisphere and block are the same, herein, $E_1 = E_2 = E$, and $\nu_1 = \nu_2 = \nu$. The maximum contact pressure, p_0, and the interference, ω, are given in the following equations:

$$p_0 = \frac{3P}{2\pi a^2} \tag{3}$$

$$\omega = \left(\frac{\pi p_0}{2E'}\right)^2 R \tag{4}$$

According to Green [35], the ratio between the maximum pressure and the maximum von Mises stress in normal elastic contact is defined by $C(\nu) = p_o/\sigma_{e-\max}$, where $C(\nu) = 1.30075 + 0.87825\ \nu + 0.54373\ \nu^2$. At the onset of yielding, the distortion energy theory asserts that $\sigma_{e-\max} = S_y$. The critical maximum pressure, $P_{0c,}$ is, therefore, replaced by the product $C(\nu)S_y$, to establish critical values via Eqs. (1)–(4). The critical contact radius, a_c, the critical load, P_c, the critical interference, ω_c, and the critical elastic strain energy, U_c, at which the maximum von Mises stress reaches the yield strength, S_y, are derived in Ref. [35]

$$a_c = \frac{\pi C S_y R}{2E'} \tag{5}$$

$$P_c = \frac{(\pi C S_y)^3 R^2}{6E'^2} \tag{6}$$

$$\omega_c = \left(\frac{\pi C S_y}{2E'}\right)^2 R \tag{7}$$

$$U_c = \frac{(\pi C S_y)^5 R^3}{60E'^4} \tag{8}$$

Note that $C(\nu)$ and S_y always appear together as a single product term representing a combined material property. By substituting the material properties of Table 1 in Eqs. (5)–(8), the said critical parameters are obtained and are listed in Table 2. The critical contact area is calculated based on a_c, $A_c = \pi\ a_c^2$. Note that the critical values of the two loading cases are vastly different. These critical values are subsequently used to normalize (i.e., generalize) results within this work.

The scheme of normalization in this work is achieved by utilizing the normalized interference, namely $1^*\omega_c$, $2^*\omega_c$, $3^*\omega_c$, while keeping the amplitude of the horizontal displacement $1^*\omega_c$ constant throughout. It allows the results to be applied to the practical situations both microscopically and macroscopically. As a displacement-controlled model, the interference and the horizontal displacement are inputs, and the normal and tangential forces

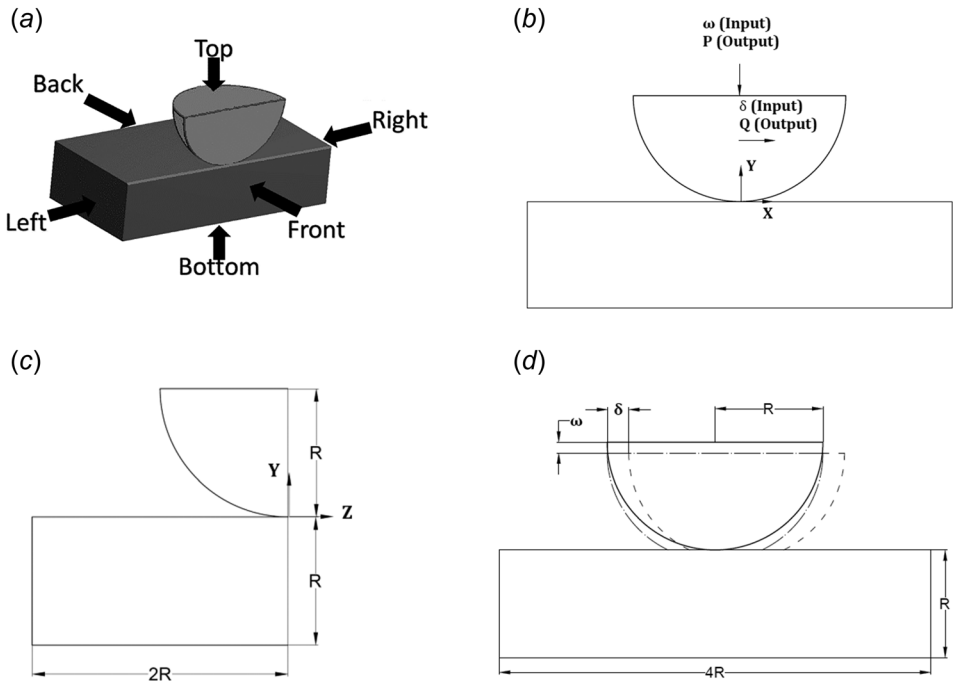

Fig. 1 Schematic of a 1/4 sphere in contact with a flat block, along with the loading definitions

are obtained as reaction forces from the software (from either ANSYS or ABAQUS).

3 Mesh

Elements Solid 186 and Solid 187 are used to mesh the model in ANSYS 17.1 (shown in Fig. 2). There are 161,830 elements. The size of the refined mesh in the contact area is 5×10^{-4}m. Approximately 6000 contact elements (CONTA174 and TARGE170) on each side of the contact are used to simulate frictionless and frictional contacts.

In order to validate the model, the mesh convergence is first performed in the regime of elastic contact for which a closed-form Hertzian solution exists [34], and the results are then compared. The following results are shown for contacts between identical steels. The same procedure is performed for the contact between an identical pair of copper with similar outcomes and for brevity these are omitted.

With the input of ω/ω_c, the interference, ω, is obtained using the aforementioned $\omega_c = 0.222$ mm. By substituting ω into Eq. (4), the maximum contact pressure, p_0, is obtained, and by using Eqs. (1)–(3), the total load applied to the contact, P, and contact radius, a, are then calculated. In the FEA simulation, with the input of the interference, ω, the total of the normal reaction force at the bottom of the block, P, the maximum contact pressure on the contacting region, p_0, and the radius of the contacting region, a, are extracted from ANSYS. The results are shown in Table 3 for steel-on-steel normal contact. Varying ω/ω_c from 0.2 to the onset of plasticity, $\omega/\omega_c = 1$, the load differs by a maximum of 2.28%, contact radius 3.70%, and maximum contact pressure 4.07%. The difference is higher when the interference is lower because extremely fine meshes are needed at lower interferences to capture the contact. However, the results are rather accurate about the $1^*\omega_c$ interference and above. Therefore, the model and mesh converge using ANSYS have been established. It is noted that for verification purposes a similar model is executed using ABAQUS with practically identical results, with similar execution times.

Since, for elastic–plastic contacts under combined normal and tangential loads, there is no closed-form solution, in that regime the elements of the mesh are iteratively refined by a factor of two until there is less than 2% difference in the contact radius between iterations.

With the converged mesh, the $4R \times 4R \times R$ flat block is scaled by a factor α in all three dimensions, ranging from 1/16 to 4, in order to verify the reasonability of taking the block as a half elastic space. The comparison between the theoretical and the numerical values at the critical interference, ω_c, is shown in Table 4, where %dif represents the relative percentage difference. In the table, the FEA results agree very well with the theoretical values when α varies from 1/2 to 4. When α is 1/4 or smaller, however,

Table 1 Material properties of steel and copper [12]

Materials	Elastic modulus (GPa) E	Yielding strength (MPa) S_y	Poisson's ratio ν
Steel	200	911.5	0.32
Copper	115	124	0.34

Table 2 The critical values for steel-on-steel and copper-on-copper contacts

Materials	$C(\nu)$	ω_c (μm)	P_c (kN)	U_c (J)	a_c (mm)	A_c (mm^2)
Steel	1.639	222	347	30.789	10.5	346.4
Copper	1.662	12.4	2.68	0.013	2.49	19.48

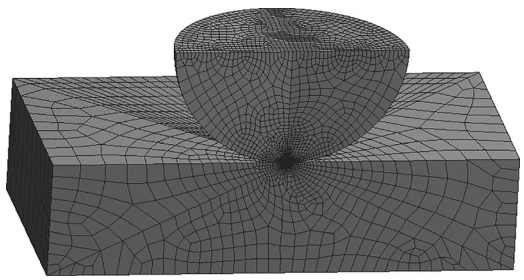

Fig. 2 Finite element model in ANSYS 17.1

Table 3 Comparison of selected values between theoretical predictions and FEA results for a hemisphere of radius, *R*, in an elastic contact with a 4R × 4R × R block

Input		Theoretical predictions				FEA results							
		Eq. (2)	Eq. (1)	Eq. (4)	p_0/C								
ω/ω_c	ω (mm)	a (mm)	P (kN)	p_0 (GPa)	σ_{emax} (GPa)	a (mm)	% dif	P (kN)	%dif	p_0 (GPa)	%dif	σ_{emax}(GPa)	%dif
0.2	0.044	4.71	31.0	0.668	0.408	4.88	3.70	30.3	−2.28	0.641	−4.07	0.393	−3.66
0.6	0.133	8.16	161	1.157	0.706	8.28	1.55	160	−0.82	1.147	−0.91	0.690	−2.33
1	0.222	10.53	347	1.494	0.911	10.6	0.65	344	−0.77	1.487	−0.47	0.899	−1.35

Note: ω ranges from 0.2*ω_c to 1* ω_c. The prediction $\sigma_{emax} = p_0/C$ is according to Green [35]. Herein, $R = 0.5$ m, $\nu_1 = \nu_2 = 0.32$, and $E_1 = E_2 = 200$ GPa.

the numerical values start to deviate from the theoretical values. The smaller the block is, the larger the deviation. In that range of $\alpha < 1/4$, the boundary conditions applied on the block affect the stress distribution in the contact region, which changes the maximum pressure, the contact area, and the load. But for $\alpha > 1/2$, the classical Saint-Venant's Principle holds. Hence, a flat block of dimensions 4R × 4R × R ($\alpha = 1$) can clearly be regarded as a half-elastic space.

4 Results and Discussion

The results of the model described earlier are presented for normalized vertical interference, $\omega^* = (\omega/\omega_c)$, ranging from 1 (the limit of the elastic regime) to 3 (in the elastic–plastic regime). Three different COFs are applied, 0, 0.3, and 1. According to the wear control handbook by Peterson and Winer [36], a COF = 0.3 is "typical" for metallic surface in dry contact, where a COF = 1 represents a high value. Therefore, with COFs = 0, 0.3, and 1, the contact conditions range from "frictionless" through "typical" to "high." Nonetheless, additional cases with different COFs have also been executed for the parametric study in forthcoming Sec. 4.6. As shown in Fig. 3, load steps are used to impose the oscillatory horizontal displacement and extract results of the intermediate state. Step 0 corresponds to the loading condition where the interference has been just applied while the hemisphere is about to move horizontally. Each cycle of the horizontal displacement is achieved by 40 loading steps. The maximum number of cycles of the oscillatory horizontal displacement is three because of the vast computational effort (132 h for a single case on a 4 cores 3 GHz personal computer with a Xeon central processing unit).

In order to describe the location and the cycle number explicitly, the following convention of notation is utilized. Points (A,B,C,D) represent, respectively, $\delta = (0,1,0,-1)\omega_c$, and the cycle number is specified by $n = 1,2,3$. For instance, A2 corresponds to the end of the first cycle, where $\delta = 0^*\ \omega_c$.

4.1 The Evolution of von Mises Stress. Figure 4 shows the evolution of the von Mises stress during three cycles of the horizontal loading at $1^*\omega_c$ with $\mu = 0.3$. Each picture is held at the same gray scale with the highest intensity representing the largest von Mises stress. The first parameter describes the view from which the distribution of the von Mises stress is given, corresponding to the views defined in Fig. 1(*a*). The next two parameters are used to identify the horizontal load step, as discussed previously. For example, Figs. 4(*a*)–4(*c*) represent the horizontal displacement of the sphere, $\delta = (0,\ 0.2,\ 1)^*\omega_c$, respectively, in branch A1–B1 (defined in Fig. 3) from the front view. Since the von Mises stress distributions in the hemisphere and the block appear as mirror images with very slight difference (caused by the geometry dissimilarity), only the progressions of the von Mises stresses in the hemisphere are discussed in the following.

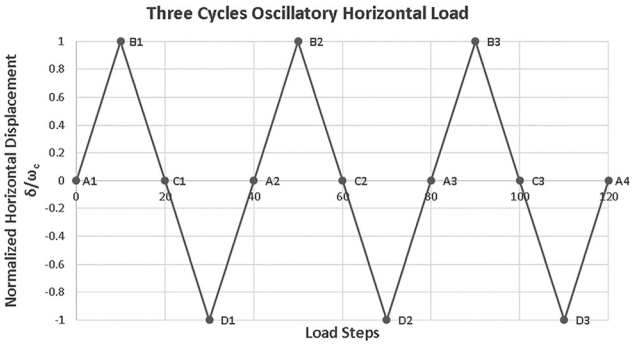

Fig. 3 Three cycles of oscillatory horizontal displacement

In order to analyze the von Mises stress under the contacting surface (where plasticity is first to appear), the distributions of the von Mises stress in the cut plane of the front view are shown in Figs. 4(*a*)–4(*h*). At the beginning, as shown in Fig. 4(*a*), there is only one point under the contacting surface reaching the yield strength in the sphere after $1^*\omega_c$ interference is just applied. It agrees with the prediction by Green [35]. Then, the hemisphere starts to move to the right as shown in Fig. 4(*b*). The region with large von Mises stresses in the hemisphere increases due to the

Table 4 Comparison of the critical values between theoretical predictions and FEA results for a hemisphere whose radius is *R*, in contact with a 4R × 4R × R block scaled by α

Scale factor α	Theoretical predictions				FEA results							
	a_c (mm)	P_c (kN)	P_{0c} (GPa)	σ_{emax} (GPa)	a_c (mm)	%dif	P_c (kN)	%dif	P_{0c} (GPa)	%dif	σ_{emax} (GPa)	%dif
1/16	10.53	347	1.494	0.9115	11.34	7.70	394	13.68	1.572	5.22	0.9864	8.22
1/8					11.08	5.25	369	6.25	1.530	2.45	0.9339	2.46
1/4					10.97	4.32	356	2.56	1.510	1.11	0.9123	0.10
1/2					10.78	2.36	350	0.86	1.501	0.52	0.9052	−0.70
1					10.60	0.65	344	−0.76	1.487	−0.46	0.8992	−1.35
2					10.74	2.01	346	−0.37	1.495	0.10	0.9008	−1.17
4					10.74	1.98	345	−0.57	1.494	0.04	0.9002	−1.24

Note: The scale factor α varied from 1/16 to 4. Herein, $R = 0.5$ m, $\nu_1 = \nu_2 = 0.32$, and $E_1 = E_2 = 200$ GPa.

introduction of the resisting tangential force. In Fig. 4(*c*), the hemisphere reaches the rightmost position, where von Mises stress on the contacting surface increases as another effect of the tangential force. Then, the hemisphere turns back to the left, where the shakedown phenomenon is observed, as shown in Fig. 4(*d*), where plasticity disappears, leaving only an elastic state. As the hemisphere slides to the further left, the largest von Mises stresses reappear under the contacting surface (Fig. 4(*e*)). The distribution of the von Mises stress stabilizes after the sphere passes the origin, and keeps that pattern until the hemisphere reaches the leftmost position (Fig. 4(*f*)). As the hemisphere turns back to the right, another shakedown appears (Fig. 4(*g*)). Then, the largest von Mises stresses again reappear under the contacting surface as the hemisphere moves back to the origin (Fig. 4(*h*)), finishing one cycle of horizontal loading. The evolution of the von Mises stresses remains the same for the second and the third cycle, with the same distributions of von Mises stress at A2, A3, and A4, as shown by ANSYS.

In addition to the front view, the bottom view of the distribution of the von Mises stresses showing the contacting surface of the hemisphere is shown in Fig. 4(*i*). Since the COF is relative small, the von Mises stress on the contacting surface is smaller than that under the surface in the bulk material and never reaches the yield strength during oscillatory horizontal loading (indicated by Fig. 4(*i*), the evolutions of the other bottom views are omitted for brevity). For this case of $1^*\omega_c$ and $\mu = 0.3$, the largest von Mises stress shows up always under the surface, where the cracks and fatigue are most likely to initiate and propagate.

However, as the COF increases, different evolutions of the von Mises stresses show up. Figure 5 depicts the evolution of the von Mises stress during three cycles of the horizontal loading at $1^*\omega_c$ with $\mu = 1$. As shown in the front view, Fig. 5(*a*), after three cycles of loading, the largest von Mises stress appears at the edges of the contact. In order to analyze the von Mises stress on the contacting surface, the bottom views of the von Mises stress distribution in the hemisphere are shown in Figs. 5(*b*)–5(*l*).

At the very being beginning just after the vertical interference is applied, the von Mises stress on the surface, as shown in Fig. 5(*b*), is relatively small, since the tangential force has not been introduced yet. Then, the hemisphere moves to the right. In Fig. 5(*c*), the large von Mises stresses form "rings" at the contacting edges. As the hemisphere slides further to the right, the "rings" spread to the center until the whole contacting area is covered by the large von Mises stresses (Fig. 5(*d*)). This is caused by continued accumulation of plastic deformation. After reaching the rightmost position (Fig. 5(*d*)), the hemisphere turns back to the left (Fig. 5(*e*)), where shakedown is apparent. As the sphere slides to the left further, the "ring" of large von Mises stresses appears at the edges of the contact again (Figs. 5(*f*)–5(*h*)). When the hemisphere reaches the leftmost position, the whole contacting area is covered by the large von Mises stresses (Fig. 5(*i*)). Seemingly, Figs. 5(*d*) and 5(*i*) are mirror images at the two extreme side positions. Then, the hemisphere turns back to the right, and another shakedown appears (Fig. 5(*j*)). As the hemisphere returns to the origin (Fig. 5(*k*)), the "rings" of large von Mises stresses show up at the contacting edges again. Comparing the distributions of von Mises stresses at the end of the first cycle and third cycle, the "rings" of large von Mises stress are stretched in the X direction, which indicates the stretching of the contacting area (discussed in Sec. 4.3). In this case, once the fretting motion commences, the largest von Mises stress stays at the edges of the contacting area, where cracking and fatigue are most likely to initiate and propagate.

A conclusion can be drawn that, with small COF, the largest von Mises stress is located under the surface, while with sufficient large COF, the largest von Mises stress shows up at the contacting surface and is located at the edge of the contact.

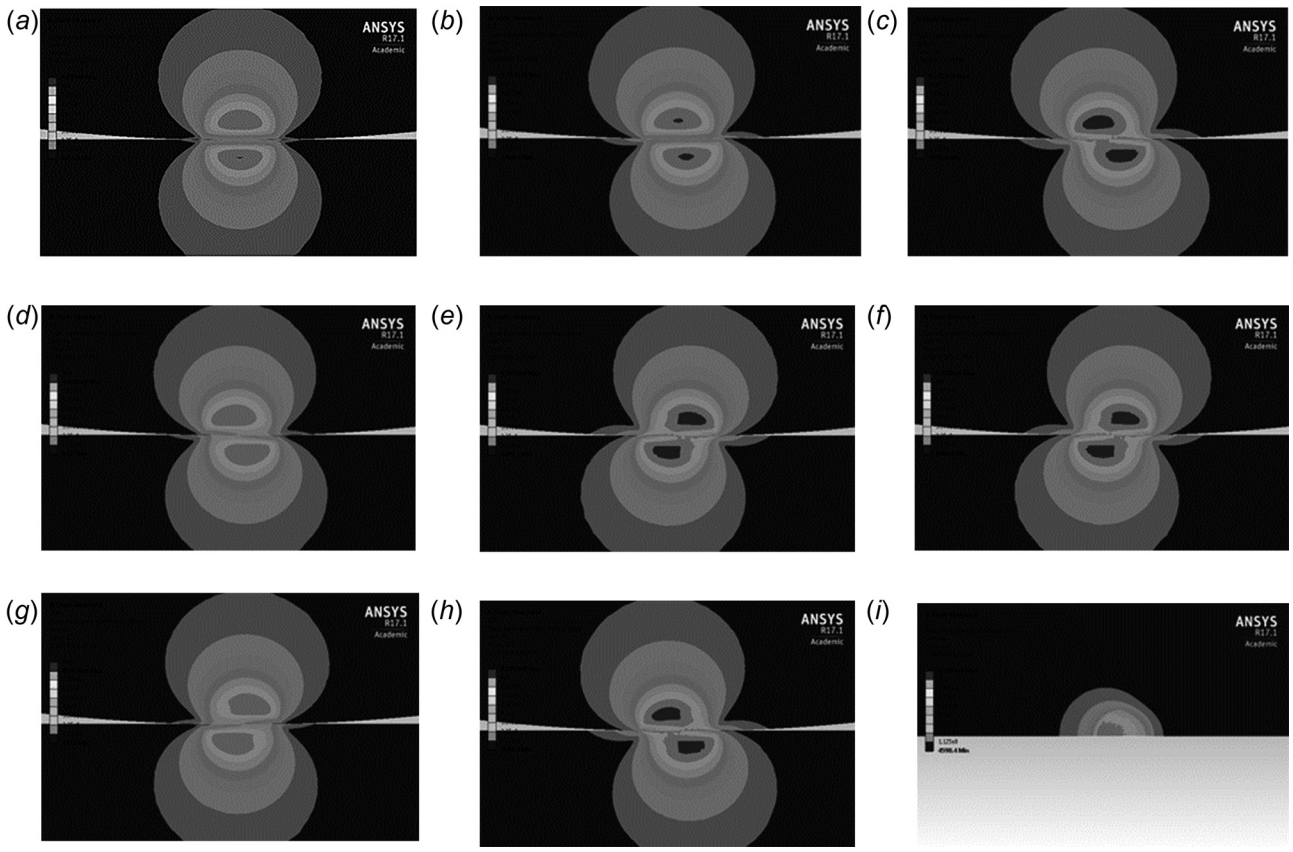

Fig. 4 The evolution of von Mises stresses during three cycles of horizontal loading at $1^*\omega_c$ interference with $\mu = 0.3$: (*a*) Front view, $0^*\omega_c$ at A1-B1, (*b*) front view, $0.2^*\omega_c$ at A1-B1, (*c*) front view, $1^*\omega_c$ at A1-B1, (*d*) front view, $0.8^*\omega_c$ at B1-C1, (*e*) front view, $0^*\omega_c$ at B1-C1, (*f*) front view, $-1^*\omega_c$ at C1-D1, (*g*) front view, $-0.8^*\omega_c$ at D1-A2, (*h*) front view, $0^*\omega_c$ at A2, and (*i*) bottom view, $0^*\omega_c$ at A4

4.2 The Evolution of the Equivalent Plastic Strain. With the von Mises stress reaching the yield strength, there are equivalent plastic strains, ε_p, appearing in the model. Figure 6 shows the evolution of the plastic strain at 1* ω_c interference with $\mu = 1$ for three cycles of horizontal loading. Figure 6(*a*) depicts the front view of the distribution of ε_p at the end of the third cycle. Evidently, the large plastic strains are located at the surface of the contact. In order to track the evolution of the plastic strain on the contacting surface, the bottom of the hemisphere during the fretting is shown in Figs. 6(*b*)–6(*h*). There is no plastic strain shown on the bottom surface until the hemisphere slides 0.4* ω_c to the right (Fig. 6(*b*)), where the earliest plastic strain appears at the edge of the contact. As the hemisphere moves further to the right, the plastic strain gradually forms a "ring" at the edges of the contact (Figs. 6(*c*)–6(*e*)). This "ring" stays there at the end of the first cycle, and it is stretched in the *X* direction just as the distribution of the von Mises stresses do in Sec. 4.2. As the fretting motion proceeds, the "ring" of the plastic strain remains at the edges of the contact (Figs. 6(*f*) and 6(*g*)), with multiple peaks, which are caused by the oscillatory motion.

The plastic strain is not found on the contacting surface for the above case when the COF drops to 0.3. Instead, there is only slight plastic strain under the surface ($\varepsilon_{pmax} = 0.001$ at A4) compared with that of the case of COF = 1 ($\varepsilon_{pmax} = 0.1$ at A4).

4.3 Junction Growth. During the fretting motion, the contact area is found to increase in some cases, which is known as the junction growth. Figure 7 shows the schematics of the contact region at 1*ω_c with $\mu = 1$. The symbol "o" represents the region at the loading step A1, i.e., at the beginning of the loading. The symbol "x" represents the region at the loading step A4, i.e., at the end of the three cycles of loading. In the figure, the contact region grows radially. However, the growth in the *X* direction is larger than that in the *Z* direction, which stretches the contact region in the *X* direction. It is corresponding to the stretch of the distribution of von Mises stresses and plastic strains in the *X* direction (Secs. 4.2 and 4.3).

In order to calculate the contact area, the trapezoidal rule is utilized to integrate the discretized data as shown in Fig. 7. Figure 8 shows the evolutions of the contact area at 1*ω_c with $\mu = 0.3$ and $\mu = 1$ during three cycles of horizontal loading. When the COF is small ($\mu = 0.3$), the von Mises stress on the contacting surface never reaches the yield strength (Sec. 4.1), which introduces no

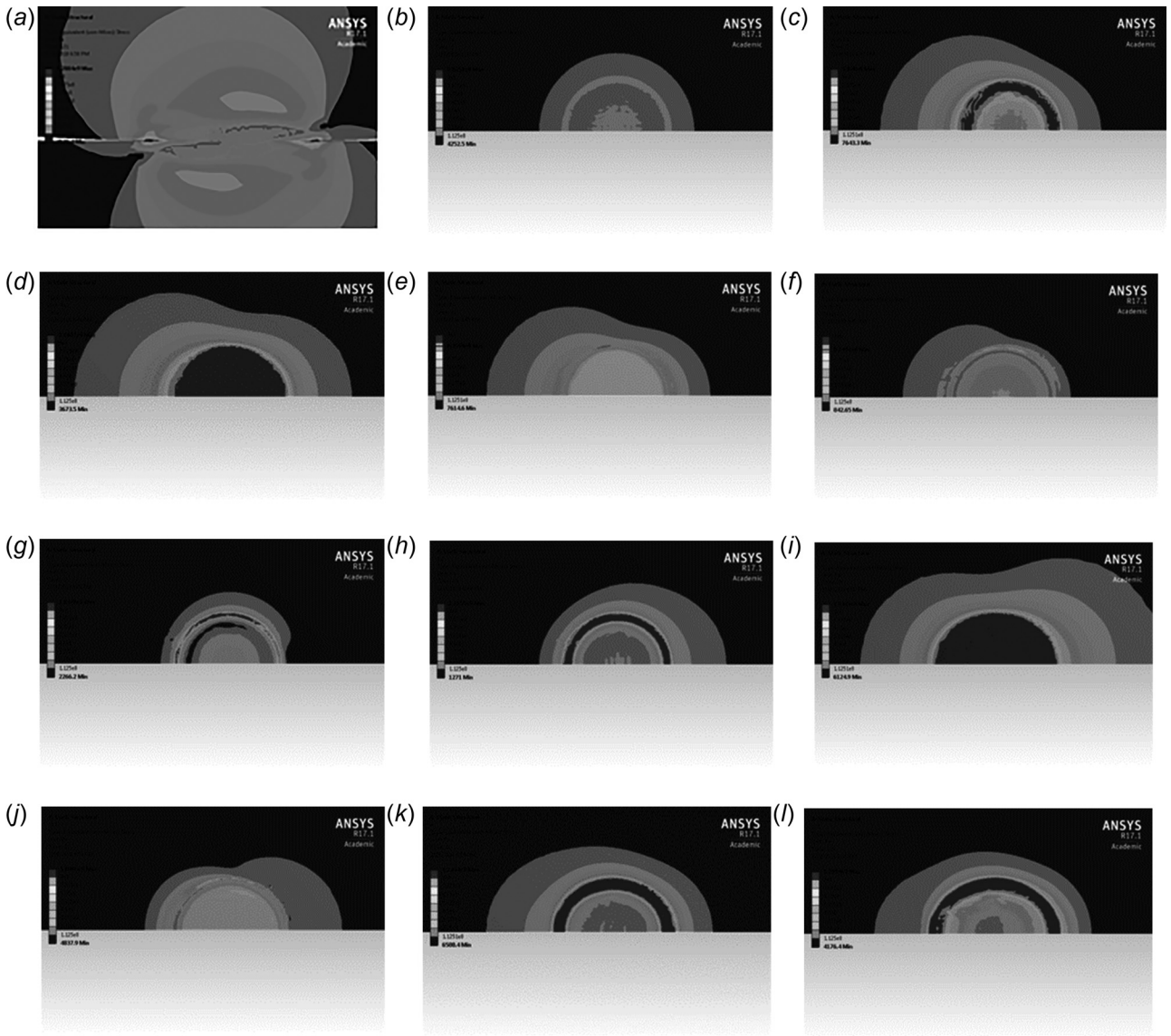

Fig. 5 The evolution of von Mises stresses during three cycles of horizontal loading at 1* ω_c interference with $\mu = 1$: (*a*) Front view, 0*ω_c at A4, (*b*) bottom view, 0*ω_c at A1, (*c*) bottom view, 0.4*ω_c at A1-B1, (*d*) bottom view, 1*ω_c at A1-B1, (*e*) bottom view, 0.8*ω_c at B1-C1, (*f*) bottom view, 0.6*ω_c at B1-C1, (*g*) bottom view, 0.4*ω_c at B1-C1, (*h*) bottom view, 0.2*ω_c at B1-C1, (*i*) bottom view, −1*ω_c at C1-D1, (*j*) bottom view, −0.6*ω_c at C1-D1, (*k*) bottom view, 0*ω_c at A2, and (*l*) bottom view, 0*ω_c at A4

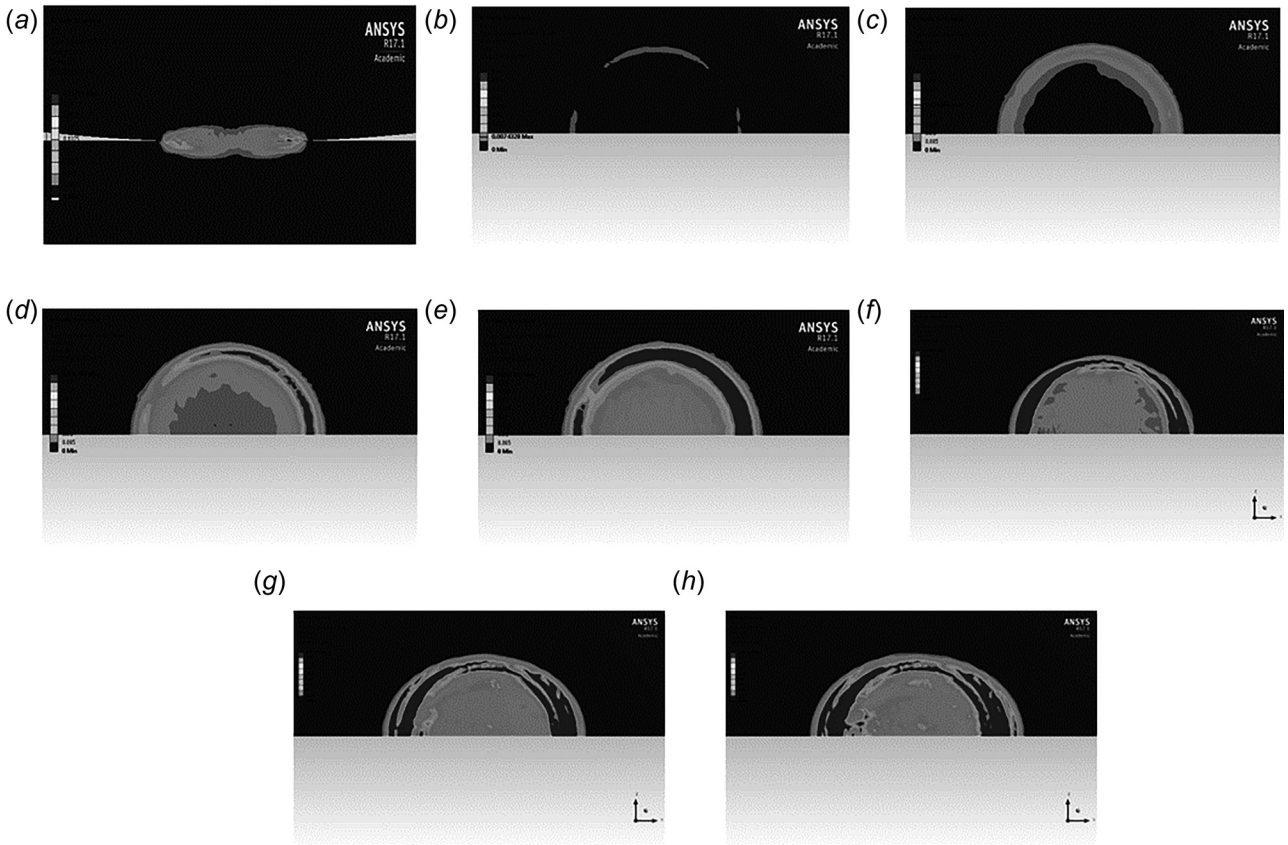

Fig. 6 The evolution of equivalent plastic strain during three cycles of horizontal loading at 1* ω_c interference with $\mu = 1$: (*a*) Front view, 0*ω_c at A4, (*b*) bottom view, 0.4*ω_c at A1-B1, (*c*) bottom view, 0.6*ω_c at A1-B1, (*d*) bottom view, 0.8*ω_c at A1-B1, (*e*) bottom view, 1*ω_c at B1, (*f*) bottom view, 0*ω_c at A2, (*g*) bottom view, 0*ω_c at A3, and (*h*) bottom view, 0*ω_c at A4

plastic deformation on the surface (Sec. 4.2). As a result, there is no junction growth at $1^*\omega_c$ with $\mu = 0.3$. However, as the COF increases to $\mu = 1$, the tangential force introduces plastic strain on the surface (Sec. 4.2), which eventually causes the junction growth, as shown in Fig. 7. The junction growth continues during three cycles of loading, and it tends to stabilize after sufficient cycles.

4.4 Scars on the Surfaces of the Block. Figure 9 shows the profile of the contacting region of the block after three cycles of horizontal loading, while the vertical interference is still maintained at $1^*\omega_c$ with $\mu = 1$ at location A4. There are pileups at the edges of the contact (see also the inset). This is due to the plasticity on the surface, introduced by the friction force. When the COF decreases to $\mu = 0.3$ with the same interference $1^*\omega_c$, there is no pileup after three cycles of horizontal loading, as shown in Fig. 10. It can be explained by the absence of plastic strain at the surface, as indicated in Sec. 4.2. When the interference increases to $3^*\omega_c$ with the COF of $\mu = 1$, the pileups show up again (Fig. 11), but they are not as pronounced as those for $1^*\omega_c$ interference (Fig. 9). The explanation is as follows. First, it should be noted that ANSYS provides specific information regarding the status of the contact, i.e., whether it is in full stick, partial slip, or gross slip. So, as the hemisphere starts to move from the original contact position, the contact status is in full stick at first, but then it goes into partial slip, and finally, it transitions to gross slip (i.e., when the local tangential stress reaches the value of COF*normal-pressure). For the cases with pileups, the contact status is full stick at the rightmost and leftmost positions. The horizontal displacement applied on the top surface of the hemisphere causes in general an elastic deformation of the bulk material and the displacement of the stick region. The smaller the displacement of the stick region is, less pronounced the scar is. With a larger interference, the stick area is more firmly fixed and it displaces less. Therefore, the larger interferences introduce less pronounced scars with the same COF.

4.5 The Evolution of the Tangential Force. Figure 12 shows the evolution of the tangential force during three cycles of horizontal loading with $\mu = 1$ at $1^*\omega_c$ interference. The tangential force (or traction), Q, is extracted from ANSYS similar to the normal force, P. Specifically, the reaction forces on the top surface of the hemisphere are summed up in the horizontal direction, and designated as Q, to be the active force necessary to displace the hemisphere as prescribed. That force, Q, is normalized by the critical load, P_c. As shown in Fig. 12, the normalized tangential force,

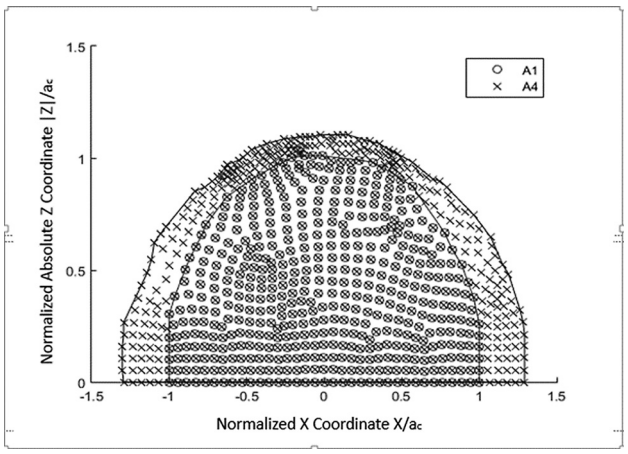

Fig. 7 The schematics of the contact zone at the beginning and ending of the three cycles (A4) of loading at 1*ω_c with $\mu = 1$

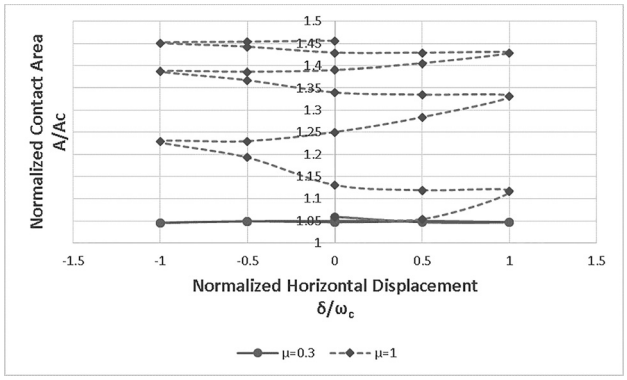

Fig. 8 The evolution of junction growth at 1*ω_c with $\mu = 0.3$ and $\mu = 1$ during three cycles of horizontal loading

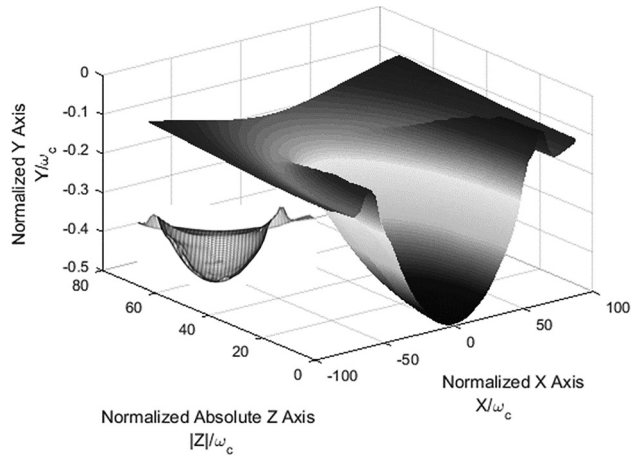

Fig. 9 The surface profile of the contacting region of the block at 1*ω_c after three cycles of horizontal loading with $\mu = 1$

Q/P_c, tends to stabilize after the first quarter of the cycle. The evolution has the similar trend of the initial few cycles of the fretting loop as reported in Ref. [37]. The enclosed area represents the work consumption during the fretting motion. The maximum normalized tangential load increases after each cycles, and tends to reach the COF applied, $\mu = 1$. It is relatively smaller than the applied COF due to the partial slip and partial stick contact conditions occurring at the rightmost and leftmost positions.

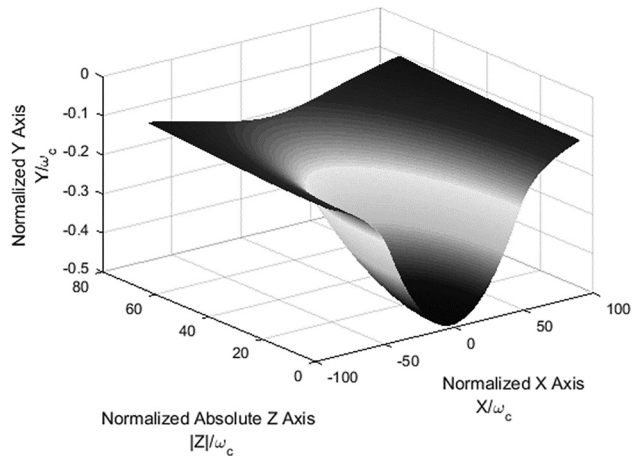

Fig. 10 The surface profile of the contacting region of the block at 1*ω_c after three cycles of horizontal loading with $\mu = 0.3$

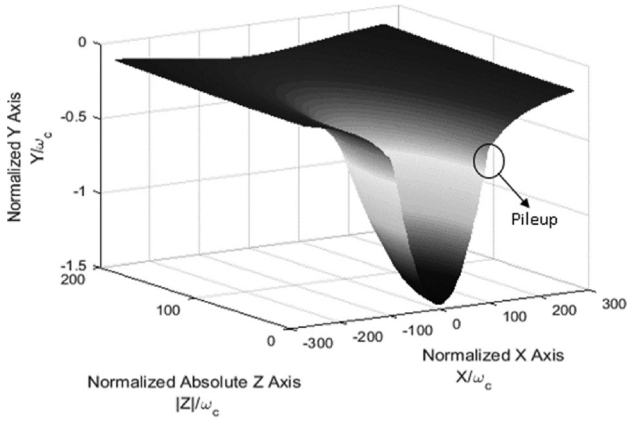

Fig. 11 The surface profile of the contacting region of the block at 3*ω_c after three cycles of horizontal loading with $\mu = 1$

When the COF decreases to 0.3, the evolution of the normalized tangential force is shown in Fig. 13 (see the loop). The loop stabilizes after the first quarter of the cycle. The evolutions of the second and the third cycles are the same, which means the fretting motion has stabilized after two cycles. Additionally, the maximum normalized tangential force, which quantitatively equals to the effective COF ($\mu_e = Q/P_c$), stabilizes at the value of the COF applied, $\mu = 0.3$. It is attributed to the full slip contact conditions (indicated by ANSYS) at the rightmost and leftmost positions.

The frictionless evolution of the tangential force at 1*ω_c is also shown in Fig. 13 (see the horizontal line). In that case, the tangential force is always zero, which means that the elastic resistance caused by the indentation is subtle. The frictionless evolutions of the tangential force are also investigated at different interferences. The tangential force stays at zero even when the interference is extended to 10* ω_c. The explanation is that since the two bodies are made of the same material, the sphere is geometrically, i.e., structurally, weaker than the block. The sphere then is deformed more, so that there is no effective plowing during the fretting motion, which leads to the zero tangential force. Therefore, when friction is present, the tangential force is generated by the frictional traction at the interface.

4.6 The Work Done to the System. As shown in Sec. 4.5, the area under hysteresis curve of the tangential force represents the work invested into the system (Figs. 12 and 13). Considering loading as quasi-static, the kinetic energy is not considered. Therefore, the work transfers to three kinds of energy: elastic strain energy, plastic strain energy, and frictional energy dissipation.

The work, U, is derived by Eq. (9), where Q is the active tangential force applied on the top surface of the hemisphere to impose δ, which is the horizontal displacement of the hemisphere

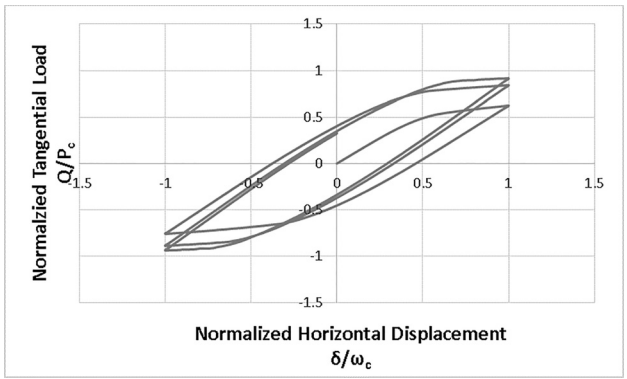

Fig. 12 The evolution of the tangential force during three cycles of horizontal loading at 1*ω_c with $\mu = 1$

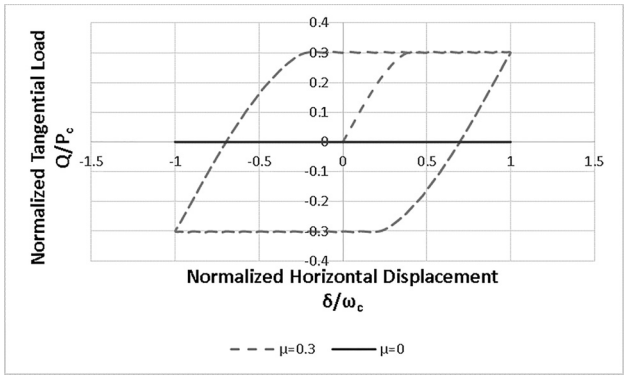

Fig. 13 The evolution of the tangential force during three cycles of horizontal loading at 1*ω_c with $\mu = 0.3$ and $\mu = 0$

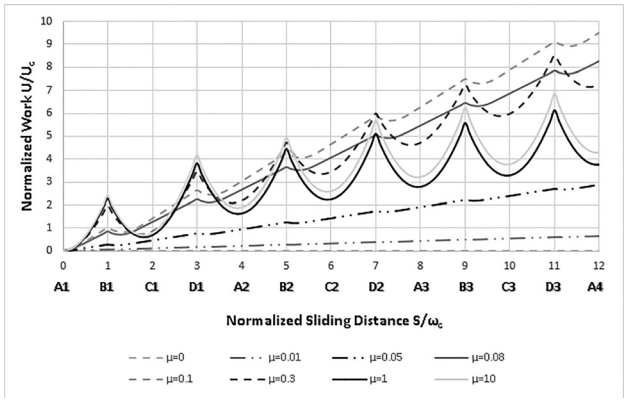

Fig. 14 The evolution of the total work done to the system at 3*ω_c during three cycles of loading with different COFs

top surface. The trapezoidal rule is utilized to integrate the discretized data extracted from ANSYS

$$U = \int Q\, d\delta \tag{9}$$

Figure 14 shows the evolution of the total work done to the system at 3*ω_c during three cycles of loading with different COFs. The work is normalized by the critical work, $U_c = 30.789$J (see Table 2). The sliding distance represents the absolute distance the hemisphere passes, and the corresponding fretting motion position

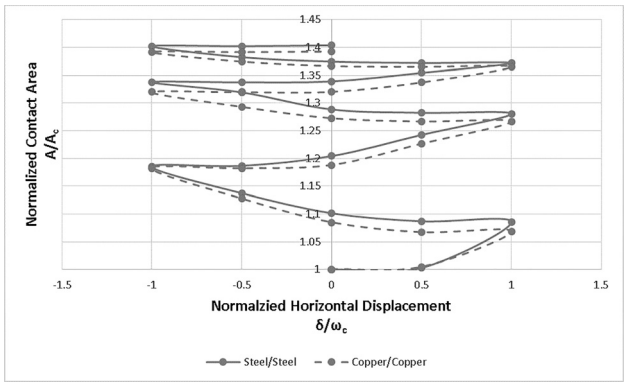

Fig. 15 The evolution of the normalized contact area during three cycles of horizontal displacement at 1*ω_c interference with the same normalized displacement input, $\mu = 1$. Note that A_c and ω_c are taken from Table 2 corresponding to steel and copper.

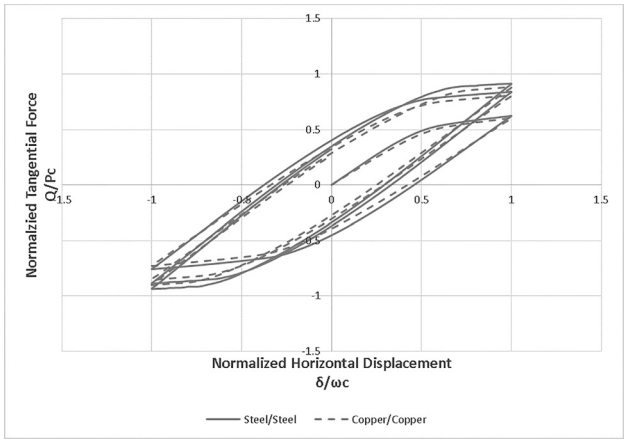

Fig. 16 The evolution of the tangential force during three cycles of horizontal displacement at 1*ω_c interference with the same normalized displacement input, $\mu = 1$. Note that P_c, and ω_c are taken from Table 2 corresponding to steel and copper.

is shown. Note that additional COFs cases are added here, including 0.001, 0.05, 0.08, 0.1, and 10. Taking the work evolution with $\mu = 0.3$ as an example, the work increases during the sliding of the hemisphere first to the right, which contains the three work forms discussed above. As the hemisphere turns back to the left at B_1, the work drops because of the release of the elastic strain energy, which is further verified by the shakedown phenomenon in Sec. 4.1. When the hemisphere approaches the origin at C_1, the effect of the elastic strain energy is overshadowed by the dissipation of frictional and plastic effects. The work starts to increase again until another shakedown occurring at D_1. The fluctuating nature of the evolution is caused by the restoration (i.e., release) of elastic strain energy, and the cumulative increase of the evolution is caused by the dissipation of the fictional and plastic effects.

As the COF increases, the elastic strain energy effect becomes dominant, and the frictional dissipation decreases since most of the contacting area during fretting is in the stick condition (as indicated by ANSYS). Therefore, comparing $\mu = 0.1$ and $\mu = 0.3$, the work done to the system is larger in case with $\mu = 0.3$ initially, but then it becomes smaller as fretting continues. As the COF decreases, the elastic strain energy effect is not dominant. But the friction dissipation decreases as a result of the drop of the COF. Therefore, at a certain interference, there exists a certain ("critical") COF, which produces the largest work dissipation.

4.7 Scheme of Normalization. In order to verify the normalization scheme utilized in this work, the normalized results, including the contact area and the tangential force, for steel-on-steel and copper-on-copper contacts are compared in Figs. 15 and 16. It is pointed that steel and copper have significantly different material properties and critical values (see Tables 1 and 2). Figure 15 depicts the evolution of the normalized contact area during three cycles of horizontal loading at 1*ω_c with $\mu = 1$. Figure 16 depicts the evolution of the normalized tangential force under the same conditions as in Fig. 15. The curves for the steel-on-steel and copper-on-copper contacts are very close. The good agreement demonstrates the effectiveness of the normalization scheme. That means that the normalized results of the fretting model for different material properties are effectively the same when normalized. In other words, it suggests that the results of this work can be applied to the fretting between materials that may be different from those investigated in the current model.

5 Conclusion

This work models a 3D contact between a hemisphere and a flat block. The materials of the two bodies are set to be identical steels with 1% strain hardening based on the elastic modulus. It is a

displacement-controlled model with various COFs being applied at the interface. Several conclusions are drawn:

(1) The largest von Mises stress is confined under the contacting surface with small COFs, while with sufficiently large COFs, the largest von Mises stress shows up at the contacting surfaces and is located at the edge of the contact.
(2) With sufficiently large COFs, the large plastic strains form multiple "rings" on the contacting surfaces after the oscillatory fretting motion.
(3) Junction growth is found when there is plastic deformation on the surface of the contact. The contacting region is stretched in the direction of the fretting motion.
(4) There are scars on the surface of the block caused by the fretting motion. There are pileups at the edges of the contact with large COF. Since the magnitude of the oscillatory sliding distance is relatively small, $1^*\omega_c$, the pileup phenomenon is not pronounced.
(5) The fretting loop of the initial cycles is found. The evolution of the tangential force stabilizes fast with small COFs. The maximum effective COF during the cyclic loading equals to the COF applied to the model after the stabilization. The tangential force is always zero at frictionless contact without the plowing effect, which is due to the sphere being structurally weaker than the block.
(6) The work done to the system equals to the enclosed area of the hysteresis curve, which is the evolution of the tangential loading. It corresponds to three kinds of energy: elastic strain energy, plastic strain energy, and frictional energy dissipation. The fluctuating nature of the evolution of the work is caused by the reservation of the elastic strain energy, while the cumulative increase of the effect is caused by the dissipation of the frictional and plastic dissipation. At certain interference, there exists a certain COF, which will yield the largest work done to the system.
(7) The current normalization scheme has been proven effective to generate results for various material properties and scales.

Funding Data

- Department of Energy under Project 2506U87, Award RH452.

Nomenclature

a = contact radius
A = contact area
a_c = critical contact radius
A_c = critical contact area
C = Poisson's ratio parameter
E = elastic modulus
E' = equivalent elastic modulus
P = normal force
p_0 = maximum contact pressure
p_{0c} = critical maximum contact pressure
P_c = critical normal force
Q = tangential force
R = radius of sphere
S = absolute sliding distance
S_y = yield strength
U_c = critical elastic strain energy
δ = horizontal displacement
ε_p = equivalent plastic strain
μ = coefficient of friction
μ_e = effective coefficient of friction
ν = Poisson's ratio
σ_e = equivalent von Mises stress
ω = interference
ω_c = critical interference
ω^* = normalized interference, ω/ω_c

References

[1] Varenberg, M., Etsion, I., and Halperin, G., 2005, "Nanoscale Fretting Wear Study by Scanning Probe Microscopy," Tribol. Lett., **18**(4), pp. 493–498.
[2] Li, G., Ding, S., Bao, M., and Sun, H., 2017, "Effect of Actively Managed Thermal-Loading in Optimal Design of an Aeroengine Turbine Disk," Int. Commun. Heat Mass Transfer, **81**, pp. 257–268.
[3] Yang, Q., Zhou, W., Gai, P., Zhang, X., Fu, X., Chen, G., and Li, Z., 2017, "Investigation on the Fretting Fatigue Behaviors of Ti–6Al–4V Dovetail Joint Specimens Treated With Shot-Peening," Wear, **372–373**, pp. 81–90.
[4] Shi, L., Wei, D-S., Wang, Y-R., Tian, A-M., and Li, D., 2016, "An Investigation of Fretting Fatigue in a Circular Arc Dovetail Assembly," Int. J. Fatigue, **82**, pp. 226–237.
[5] Chan, K. S., Enright, M. P., Moody, J. P., Golden, P. J., Chandra, R., and Pentz, A. C., 2010, "Residual Stress Profiles for Mitigating Fretting Fatigue in Gas Turbine Engine Disks," Int. J. Fatigue, **32**(5), pp. 815–823.
[6] Vingsbo, O., and Söderberg, S., 1988, "On Fretting Maps," Wear, **126**(2), pp. 131–147.
[7] Varenberg, M., Etsion, I., and Halperin, G., 2004, "Slip Index: A New Unified Approach to Fretting," Tribol. Lett., **17**(3), pp. 569–573.
[8] Hoeppner, D., Adibnazari, S., and Moesser, M. W., 1994, "Literature Review and Preliminary Studies of Fretting and Fretting Fatigue Including Special Applications to Aircraft Joints," Utah University, Salt Lake City, UT, Report No. DOT/FAA/CT-93/2.
[9] Chivers, T., and Gordelier, S., 1985, "Fretting Fatigue and Contact Conditions: A Rational Explanation of Palliative Behaviour," Proc. Inst. Mech. Eng., Part C, **199**(4), pp. 325–337.
[10] Courtney-Pratt, J., and Eisner, E., 1957, "The Effect of a Tangential Force on the Contact of Metallic Bodies," Proc. R. Soc. London A, **238**(1215), pp. 529–550.
[11] Parker, R., and Hatch, D., 1950, "The Static Coefficient of Friction and the Area of Contact," Proc. Phys. Soc. Sect. B, **63**(3), p. 185.
[12] Tabor, D., 1959, "Junction Growth in Metallic Friction: The Role of Combined Stresses and Surface Contamination," Proc. R. Soc. London A: Math., Phys. Eng. Sci., **251**(1266), pp. 378–393.
[13] Leonard, B. D., Sadeghi, F., Evans, R. D., Doll, G. L., and Shiller, P. J., 2009, "Fretting of WC/aC: H and Cr2N Coatings Under Grease-Lubricated and Unlubricated Conditions," Tribol. Trans., **53**(1), pp. 145–153.
[14] Leonard, B. D., Sadeghi, F., Shinde, S., and Mittelbach, M., 2012, "A Novel Modular Fretting Wear Test Rig," Wear, **274–275**, pp. 313–325.
[15] Warhadpande, A., Leonard, B., and Sadeghi, F., 2008, "Effects of Fretting Wear on Rolling Contact Fatigue Life of M50 Bearing Steel," Proc. Inst. Mech. Eng., Part J, **222**(2), pp. 69–80.
[16] Zhu, M., Zhou, Z., Kapsa, P., and Vincent, L., 2001, "Radial Fretting Fatigue Damage of Surface Coatings," Wear, **250**(1–12), pp. 650–657.
[17] Xu, J., Zhu, M., Zhou, Z., Kapsa, P., and Vincent, L., 2003, "An Investigation on Fretting Wear Life of Bonded MoS2 Solid Lubricant Coatings in Complex Conditions," Wear, **255**(1–6), pp. 253–258.
[18] Jin, X., Sun, W., and Shipway, P., 2016, "Derivation of a Wear Scar Geometry-Independent Coefficient of Friction From Fretting Loops Exhibiting non-Coulomb Frictional Behaviour," Tribol. Int., **102**, pp. 561–568.
[19] Eriten, M., Polycarpou, A., and Bergman, L., 2010, "Physics-Based Modeling for Partial Slip Behavior of Spherical Contacts," Int. J. Solids Struct., **47**(18–19), pp. 2554–2567.
[20] Eriten, M., Polycarpou, A., and Bergman, L., 2011, "Physics-Based Modeling for Fretting Behavior of Nominally Flat Rough Surfaces," Int. J. Solids Struct., **48**(10), pp. 1436–1450.
[21] Kogut, L., and E, I., 2002, "Elastic–Plastic Contact Analysis of a Sphere and a Rigid Flat," ASME J. Appl. Mech., **69**(5), pp. 657–662.
[22] Jackson, R. L., and Green, I., 2005, "A Finite Element Study of Elasto-Plastic Hemispherical Contact Against a Rigid Flat," ASME J. Tribol., **127**(2), pp. 343–354.
[23] Tsukizoe, T., and Hisakado, T., 1968, "On the Mechanism of Contact Between Metal Surfaces—Part 2: The Real Area and the Number of the Contact Points," ASME J. Lubr. Technol., **90**(1), pp. 81–88.
[24] Holmberg, K., Laukkanen, A., Ronkainen, H., Wallin, K., Varjus, S., and Koskinen, J., 2006, "Tribological Contact Analysis of a Rigid Ball Sliding on a Hard Coated Surface—Part I: Modelling Stresses and Strains," Surf. Coat. Technol., **200**(12–13), pp. 3793–3809.
[25] Moody, J. J., 2007, "A Finite Element Analysis of Elastic-Plastic Sliding of Hemispherical Contacts," M.S. thesis, Georgia Institute of Technology, Atlanta, GA.
[26] Green, I., 2018, "An Elastic-Plastic Finite Element Analysis of Two Interfering Hemispheres Sliding in Frictionless Contact," Phys. Sci. Int. J., **19**(1), pp. 1–34.
[27] Boucly, V., Nelias, D., and Green, I., 2007, "Modeling of the Rolling and Sliding Contact Between Two Asperities," ASME J. Tribol., **129**(2), pp. 235–245.
[28] Gupta, V., Bastias, P., Hahn, G. T., and Rubin, C. A., 1993, "Elasto-Plastic Finite-Element Analysis of 2-D Rolling-Plus-Sliding Contact With Temperature-Dependent Bearing Steel Material Properties," Wear, **169**(2), pp. 251–256.

[29] Ghosh, A., Leonard, B., and Sadeghi, F., 2013, "A Stress Based Damage Mechanics Model to Simulate Fretting Wear of Hertzian Line Contact in Partial Slip," Wear, **307**(1–2), pp. 87–99.
[30] Yang, H., and Green, I., 2018, "An Elastoplastic Finite Element Study of Displacement-Controlled Fretting in a Plane-Strain Cylindrical Contact," ASME J. Tribol., **140**(4), p. 041401.
[31] Yang, H., and Green, I., 2018, "A Fretting Finite Element Investigation of a Plane-Strain Cylindrical Contact of Inconel 617/Incoloy 800H at Room and High Temperature," Proc. Inst. Mech. Eng. Part J (epub).
[32] Zolotarevskiy, V., Kligerman, Y., and Etsion, I., 2011, "Elastic–Plastic Spherical Contact Under Cyclic Tangential Loading in Pre-Sliding," Wear, **270**(11–12), pp. 888–894.
[33] Shi, X., Wu, A., Zhu, C., and Qu, S., 2013, "Effects of Load Configuration on Partial Slip Contact Between an Elastic Plastic Sphere and a Rigid Flat," Tribol. Int., **61**, pp. 120–128.
[34] Johnson, K. L., 1987, *Contact Mechanics*, Cambridge University Press, Cambridge, UK.
[35] Green, I., 2005, "Poisson Ratio Effects and Critical Valus in Spherical and Cylindrical Hertzian Contacts," Appl. Mech. Eng., **10**(3), p. 451.
[36] Peterson, M. B., and Winer, W. O., 1980, *Wear Control Handbook*, American Society of Mechanical Engineers, New York.
[37] Walvekar, A. A., Leonard, B. D., Sadeghi, F., Jalalahmadi, B., and Bolander, N., 2014, "An Experimental Study and Fatigue Damage Model for Fretting Fatigue," Tribol. Int., **79**, pp. 183–196.